Pulsatile spiral blood flow through arterial stenosis

Fabian Linge, Md Abdul Hye and Manosh C. Paul[1]

CFD Group, System, Power & Energy Research Division, School of Engineering, University of Glasgow, Glasgow G12 8QQ, UK

Abstract

Pulsatile spiral blood flow in a modelled three-dimensional arterial stenosis, with a 75% cross sectional area reduction, is investigated by using numerical fluid dynamics. Two-equation k-ω model is used for the simulation of the transitional flow of Reynolds numbers 500 and 1000. It is found that the spiral component increases the static pressure in the vessel during the deceleration phase of the flow pulse. Additionally, spiral component reduces the turbulence intensity and wall shear stress found in the post stenosis region of the vessel in the early stages of the flow pulse. Hence the findings agree with the results of Stonebridge et al. (Stonebridge, Buckley, Thompson, Dick, Hunter, & Chudek, 2004). Additionally, the results of the effects of a spiral component on time-varying flow are presented and discussed along with the relevant pathological issues.

Keywords

Pulsatile blood flow; Swirl flow; Spiral; Arterial stenosis; Turbulence

[1] Corresponding author: Email: Manosh.Paul@glasgow.ac.uk, Tel: +44 (0)141 330 8466, Fax: +44 (0)141 330 4343

1 Introduction

Heart attack and stroke are leading causes of death in the Western World (Leys, 2001). The hemodynamics in blood vessels of the human circulatory systems is closely linked to the causes of such cardiovascular diseases; hence the study of blood flow dynamics is of great interest.

In-vivo research of Stonebridge (Stonebridge, Spiral laminar flow in arteries?, 1996) showed that the blood flow through the arteries is a helical spiral type flow due to the twisting of the heart about its own axis. Stonebridge further remarks that this spiral component of blood flow has both beneficial and detrimental effects in the human circulatory system.

A large amount of research on laminar hemodynamics has been conducted previously, however, the effects of the spiral component are not well known so far. Hence it is clear that simulation of spiral flow through stenosis needs further study.

Early experimental studies were mostly conducted in-vitro and using laser Doppler techniques whilst later moving on to echo magnetic resonance techniques. These investigations provide data which we still use for validation of our numerical investigations. Studies regarding steady flow through axisymmetric stenosis were carried out by Ahmed and Giddens (Ahmed & Giddens, 1983) using laser Doppler anemometry and flow visualization. They investigated the effects of various degrees of stenosis reduction on the velocity fields within the vessel for flows ranging *Re* (Reynolds number) from 500 to 2000. Results highlighted the occurrence of turbulent flow conditions downstream of higher degree of stenosis and Reynolds number.

Using standard colour Doppler techniques of three dimensional in-vivo flows Stonebridge et al. (Stonebridge, Spiral laminar flow in arteries?, 1996) investigated bi-planar arterial blood flow patterns. All the flow patterns sampled showed stable rotational flow in varying direction. The report concluded with possible theoretical advantages of spiral laminar flow reducing laterally directed forces, reducing turbulence in vessels containing stenosis and effecting mechanisms of endothelial damage and repair.

Further Stonebridge et al. (Stonebridge, Buckley, Thompson, Dick, Hunter, & Chudek, 2004) continued investigating spiral laminar flows using gradient echo magnetic resonance imaging and computational fluid dynamics (star CD), imposing both spiral and non-spiral flows through stenosis and unstenosed vessels. Their findings showed no difference in flow pattern in the unstenosed vessel, however in the stenosed vessel the spiral flow showed to preserve flow velocity coherence and concluded that the spiral flow had clear profile stabilizing advantages over the non-spiral case.

With the advancement of computing power computational fluid dynamic techniques have become powerful tools in the study of hemodynamics. Initial computational work into blood flow which included turbulence modelling was conducted by Galichi et al. (Ghalici, Deng, De Chamlain, Douvill, King, & Guidoin, 1998). The k-ω turbulence model was used to analyse transitional or turbulent flow distal to arterial stenosis over a range of physiologically representative Reynolds numbers. The study showed good correlation between computational results and experimental data collected previously and provided good evidence of the suitability of the k-ω model for blood flow problems.

Further work was carried out by Lee et al. (Lee, Liao, & Low, 2003) where the k-ω model was again implemented to investigate parabolic turbulent blood flow imposed through a series of axisymmetric stenosis. It was concluded again that in the laminar flow region the numerical solutions provided by the k-ω model matched those given by the laminar flow modelling, suggesting that the k-ω model is good enough to predict both laminar and turbulent flow in stenosed vessels. Later work conducted by Paul et al. (Paul, Molla, & Roditi, 2009) on Large-Eddy simulation of pulsatile blood flow through a 3D model stenosis highlighted weakness in the RANS models. Only time-averaged results can be obtained from the k-ω model instead of instant results, which makes the k-ω model unpopular for pulsatile flow simulation. However, recent published papers showed that the k-ω model could be useful at predicting transitional pulsatile flows at a choice of relatively low Reynolds numbers (Ryval, Straatman, & Steinman, 2004) (Tan, et al., 2008).

Work into the effects of different shapes of stenosis on unsteady Newtonian flow was done by Sarifuddin et al. (Sarifuddin, Chakravarty, Mandal, & Layek, 2008) which concluded that the post-stenotic flow behaviour is largely dependent upon the shape of the stenosis itself with cosine, irregular and smooth shapes being considered under the investigation.

Paul and Larman (Paul & Larman, 2009) conducted work which investigates the effects of different magnitudes of spiral component in arterial stenosis using a 3D *k-ω* turbulence model for flows of Reynolds number 500 and 1000. The paper highlights significant differences observed on wall shear stresses for non-spiral and spiral cases, additionally increases in pressure and velocity were found present in the spiral cases and the work draws relevant pathological conclusions.

The objective of this piece of work is to progress the understanding of spiral blood flow by conducting numerical simulation of blood flow through a 75% area reduction stenosis arterial geometry using the Wilcox's *k*-omega turbulence model (Wilcox, 1993) and to develop results for the transient, time–varying flow case by the use of computational fluid dynamic techniques. The numerical formulation of the model and the numerical methods are summarised in Sections 2 and 3 respectively. Section 4 presents results and relevant discussion, whilst a general conclusion to the work is drawn in Section 5.

2 Problem Formulation

The blood vessel including its stenosis under investigation is modelled as a three-dimensional axisymmetric tube which is shown along with all its dimensions in Figure 1. The geometry of the stenosis is defined by the cosine function;

$$\frac{r(x)}{R} = 1 - \delta_c \left[1 + \cos\left(\frac{x\pi}{D}\right)\right], -D \leq x \leq D, \quad (1)$$

where *r* and *x* are the radial and axial coordinates respectively, and *R* and *D* are the radius and diameter of the unstenosed vessel. δ_c is a constant which controls the area reduction of the tube, in the case of this investigation δ_c is given as 0.25 resulting in a 75% reduction of the cross-sectional area at the centre of the stenosis. The length of the inlet zone is 40 mm or 4D, if normalised by the vessel diameter, the length of the stenosed zone is 20 mm or 2D and the

downstream length of the model is 210 mm or 21D, giving an overall length of 270 mm. The diameter taken in this study is typical of femoral or carotid artery.

The flow domain was meshed using the meshing software Gambit 2.4 (Fluent, 2007) with a boundary layer attached to the wall of the vessel. A gradient scheme was also applied along the axial direction of the model so that the finest mesh is found in the throat and immediately downstream of the stenosis with a gradually coarsening mesh as you move downstream, keeping computational cost to a minimum.

The principal laws of the conservation of mass and momentum govern the three dimensional fluid motion. In large arteries such as the one under investigation in this model, blood can be assumed to behave as a Newtonian fluid (Lam, Fung, Cheng, & Chow, 2008) and hence the continuity equation and the Reynolds averaged Navier-Stokes equations can be written in tensor form as;

$$\frac{\partial u_i}{\partial x_i} = 0, \tag{2}$$

$$\frac{\partial}{\partial t}(\rho u_i) + \frac{\partial}{\partial x_j}(\rho u_i u_j) = -\frac{\partial p}{\partial x_i} + \frac{\partial}{\partial x_j}\left[\mu\left(\frac{\partial u_i}{\partial x_j} + \frac{\partial u_j}{\partial x_i}\right)\right] + \frac{\partial \tau_{ij}}{\partial x_j}, \tag{3}$$

where u_i (i=1,2,3) are the components of the velocity, p is the pressure and ρ is the fluid density. The Reynolds stresses τ_{ij} are modelled by the Boussinesq hypothesis as follows:

$$\tau_{ij} = -\rho\langle u_i' u_j' \rangle = \mu_t\left(\frac{\partial u_i}{\partial x_j} + \frac{\partial u_j}{\partial x_i}\right) - \frac{2}{3}\rho k \delta_{ij}, \tag{4}$$

where u_i' are the fluctuating velocity components; $k = 0.5\langle u_i' u_j' \rangle$ is the turbulent kinetic energy; and μ_t is the turbulent viscosity. This allows modelling of momentum transfer caused by turbulent eddies with an eddy viscosity. Using the Boussineesq hypothesis to model the Reynolds stress tensor raises the need for a two equation turbulence model to be used enabling closure of the governing equations. Wilcox's standard k-ω model with a near-wall modification is applied for increased accuracy at low Reynolds numbers flow near the vessel boundaries (Fluent, 2007).

In order to simplify modelling it is assumed that the rheological properties of the fluid are kept within the range where the blood through the model can be said to be an incompressible,

Newtonian and homogeneous fluid (Ku, 1997). Hence the dynamic viscosity of the blood flow μ, is assumed to be constant at 0.00371 Nsm^{-2} and blood density ρ which is also assumed to be constant, has been taken to be 1,060 kgm^{-3} (Ku, 1997).

The arterial vessel is also simplified for the purpose of modelling by assigning no-slip boundary conditions along the vessel wall and considered to be a rigid, impermeable and perfectly circular tube. These assumptions mean that the model is subject to similar flow conditions to those found when conducting in-vitro experiments in glass apparatus (Ahmed & Giddens, 1983).

3 Numerical Simulations

A 3-D axial velocity, $\vartheta_a(y,z)$, is applied at the inlet, where the magnitude of the bulk stream-wise velocity, $V(t)$, varies with time and is controlled by a physiologically representative pulsatile velocity waveform, shown in Figure 2 (a) and taken from the experimental data of Lam et al. (Lam, Fung, Cheng, & Chow, 2008). The controlling waveform is scaled such that the peak velocity magnitude corresponds to a flow of Reynolds number of 500 and 1000. The period is 1 second per cycle (that gives 60 heart beats per minutes), and the peak flow occurs at 0.25 sec whilst the peak pressure occurs at 0.3 seconds (see Figure 2b). Hence the time-dependent inlet axial velocity is defined by the following relation:

$$\vartheta_a(y,z) = 2V(t)\left[1-\left(\frac{r}{R}\right)^2\right]. \quad (5)$$

The spiral component of the flow is applied to the inlet as a component of tangential velocity ϑ_t and is related to the bulk streamwise velocity, $V(t)$, by a controlling constant, C, which in most cases of real blood flow and throughout this investigation takes the value of $\frac{1}{6}$ (Stonebridge, Buckley, Thompson, Dick, Hunter, & Chudek, 2004). The tangential velocity is hence defined by the following relation:

$$\vartheta_t = C * V(t)\left(\frac{r}{R}\right). \quad (6)$$

No-slip condition is applied to wall. Hence the tangential velocity defined in Equation (6) is zero at the wall and centre, however it is maximum near the wall.

A time-dependent pressure profile, shown in Figure 2 (b), is applied at the downstream end of the pipe. The turbulence characteristics of the inlet flow are defined by the inlet turbulence intensity and hydraulic diameter of the pipe. Turbulence Intensity, *I*, is determined as a function of the flow Reynolds number, $I = \frac{1}{6}(Re)^{-\frac{1}{8}}$, and the hydraulic diameter of the pipe is, specifically in the case of the axisymmetric circular pipe, equal to the geometric diameter.

A pressure based implicit solver was applied to solve iteratively the governing equations which were discretised to form a system of algebraic equations by using the finite volume method. In the discretisation process, the second order upwind scheme was used for the equations of momentum, turbulent kinetic energy (k) and specific dissipation rate (ω); while the second order accurate scheme was used for the Poisson-like pressure equation formed to couple the velocity with the pressure field according to the SIMPLE method described by Patankar and Spalding (Patankar & Spalding, 1972). The inlet boundary conditions (5-6) for the streamwise velocity and the spiral speed and the outlet pressure waveform were written in C-language using the interface of User Defined Function (UDF) of Fluent and linked with the solver. The solution process was initiated from the inlet and the convergence criteria for the solutions was defined as the residuals, of each equation being solved, reducing to 10^{-4}. And a timestep size of 5×10^{-3} was used throughout the simulations.

4 Results and Discussion

A mesh independence test was conducted to ensure that the numerical solutions are independent of the geometrical mesh arrangement employed. An initial mesh of 491,000 control volumes was used, the next mesh volume increased by about 25% resulting in a larger mesh of 609,000 volumes and for the final mesh the resolution was increased by a further 100% resulting in a mesh with a massive 1,180,000 elements. For each mesh simulations were run using a steady parabolic flow of Reynolds number 500 and 1000, and the results along with a comparison against the experimental data of Ahmed and Giddens (Ahmed & Giddens, 1983) are shown in Figure 3.

It is clear from Figure 3 that the created computational mesh predicts the flow field very accurately at and near the throat of the stenosis, with an increased variance found in the experimental data moving downstream. Particularly, the axial velocity at the centre for *Re* = 500 always shows an under-prediction towards the downstream. Increasing the mesh resolution by 100% does not seem to improve the results significantly along the centreline in this case; however the velocity profiles and characteristics are predicted with good accuracy by all the three mesh resolutions. Comparatively, the velocity profiles for *Re* = 1000 obtained by both Grid2 and Grid3 show a better agreement with the experiment data, and with regards to keeping the computational costs to a minimum and still providing a high level of accuracy, Grid2 containing 609,000 control volumes is used.

Moreover, in order to determine whether a time-steady (statistically stationary) solution has been reached the fluctuation convergence through the first six velocity pulse cycles is plotted in Figure 4. The fluctuation magnitude is defined by measuring variables, at peak velocity, at a designated point on the centre-line z = 4D, then determining the values distance from the phase-average measured throughout all the cycles and expressed as a percentage. Mathematically it is expressed as $100\left(1-\frac{f}{<f>}\right)$ where f is a generic variable and $<f>$ represents its phase-averaged quantity. The convergence graphs for the flows with the Reynolds number of 500 in Figure 4 (a) and (b) show that the fluctuation converges roughly after 5 cycles; whilst the fluctuations in the Reynolds number 1000 case, shown in Figure 4 (c) and (d), are relatively quicker to converge and an approximate time-steady solution is reached after only 3 cycles. During the analysis of further simulation results data is recorded during the 5^{th}simulation cycle and assumed to be the time-periodic solution.

In Figures Figure 5 and Figure 6, the variation of static pressure, axial velocity, tangential velocity, and radial velocity along the centre line of the vessel is plotted at various key times (t = 4.25s, 4.30s, 4.40s and 4.60s) during the flow cycle for each of the four flow scenarios such as *Re* = 500, *Re* = 500 Non-Spiral, *Re* = 1000 and *Re* = 1000 Non-Spiral. In general, the plots of the static pressure in Figure 5 show a little variation between the spiral and non-spiral cases early in the flow pulse, however, once the flow time reaches 4.60s, which is close to the mid-diastole phase, differences appear. Particularly, in the *Re* = 500 Non-Spiral case, the pressure along the

entire centreline is significantly less than in the nominal spiral case but the profile shape is similar (frame d). In the *Re* = 1000 case a large dip in pressure appears about the throat of the stenosis with an initial rapid increase followed by a gradual increase in pressure the rest of the length of the vessel. However, in the corresponding non-spiral case the pressure in the inlet is much higher, there is no dip at the throat and the pressure in the downstream gradually increases. In general the spiral flow seems to create a greater pressure through the immediate downstream of the stenosis region, towards the end of the pulse cycle (frame d).

The corresponding axial velocity profiles, presented in Figure 6, show little differences in the *Re* = 500 case with an exception of a slight decrease in the magnitude upstream of the stenosis in the inlet section in the spiral case. The same can be seen in the *Re* = 1000 case where, in general, the spiral effect causes the magnitude of the blood velocity fall before the stenosis. However, the effects of spiral in *Re* = 1000 are prominent during the diastole phase for time 4.30s onwards. Particularly, there is a significant reduction in the peak axial velocity between immediately downstream of the stenosis of the spiral case compared to the Non-Spiral case at t = 4.40s.

Interestingly, similar trends are displayed in the results for the radial velocity plots. In the first two time instances there are few discrepancies between the spiral and non-spiral cases apart from a slight reduction in magnitude of the post-stenosis peak in the *Re* = 1000 case compared to the *Re* = 1000 Non-Spiral scenario. But at t = 4.40s, differences are larger. Immediately at the post stenosis, the first peak in the *Re* = 1000 case (at approx. z = 0.025 m) is approximately twice the magnitude and of the opposite direction to that of the *Re* = 1000 Non-Spiral case. Further downstream the two profiles seem to align again and the second peak at around z = 0.1 m is fairly similar for both cases. In the last frame at t = 4.60s, the mid-stenosis peak for both *Re* = 500 and 1000 is significantly larger in the non-spiral case compared to the spiral case. There is also a secondary peak which occurs in both *Re* = 500 cases at z = 0.075 m, which does not seem to occur in the *Re* = 1000 cases.

The most dominant effects of spiral are found in the tangential velocity, as possibly expected, since the spiral component of the velocity at the inlet was applied to the tangential direction. In both the spiral cases of *Re* = 500 and 1000, the magnitude of the tangential velocity from the

inlet drops at the first two time frames for 4.25s and 4.30s and diminishes towards the far downstream of the stenosis. In terms of the profile shapes and manners, these are quite similar for *Re* = 500 and 1000 in the first two time frames. However, in the third time frame, where *t* = 4.40s, there is a significant rise to the peak at the post stenosis found in the *Re* = 1000 case which does not exist in the corresponding *Re* = 500 case. Interestingly, though the peak occurring at about the same post stenosis location in the fourth frame at *t* = 4.60s, there is a sudden drop in the tangential velocity predicted in the pre-lip location of the stenosis for both *Re* = 1000 and 500 cases.

Turbulence intensity gives a good measure of the instability of the flow and its variation along the centerline, at different times, is shown in Figure 7 (left). Throughout all of the sampled flow times it is clear that the turbulence intensity for the spiral cases has less magnitude than that of the non-spiral flow case. Whilst in the *Re* = 1000 case the two profiles have similar shapes, but different magnitudes, in the *Re* = 500 case there is a larger difference. Specifically, at *t* = 4.25s and 4.30s there is a clear peak in the turbulence intensity immediately downstream of the stenosis in the case of non-spiral flows which is not found in the spiral case.

Generally, the turbulence intensity profiles show a lower level of turbulence for the spiral cases throughout the pulse cycle with the trend being amplified at the lower Reynolds number flow. This pattern clearly indicates that the spiral effect has a stabilizing effect on the flow downstream of the stenosis and could reduce the potential damage done by the turbulence to the blood-cell materials in the stenosed artery (Ku, 1997).

Wall shear stresses were calculated using a circumferential average approach and plotted as a function of length along the vessel, also shown in Figure 7 (right). The shear stress profiles at time *t* = 4.25s and 4.30s show little discrepancies among the results between the spiral and non-spiral, however at time *t* = 4.40s the magnitude of the post stenosis peak in the *Re* = 1000 case is significantly greater than that of the equivalent non-spiral case. Moving on the flow time to *t* = 4.60s the results show that in the same *Re* = 1000 case now in the region immediately downstream of the stenosis the shear stress is in fact less in the spiral case, opposite to that observed in the previous time step. Additionally, the spiral flow reduced the shear stresses

upstream, and the profiles for the *Re* = 500 cases show very limited discrepancies throughout the flow cycle in the stenosis throat as well as in the downstream regions of the vessel.

Flow pathlines, where the particles are released from the inlet, are presented in Figure 8 at the four different times, previously used, for each flow situation to see the effects of spiral on the separated blood flow downstream from the throat of the stenosis. Throughout the plots there is a clear change in the structure in the recirculation region and flow structure induced by the spiral component. When regarding the pathlines taken at the four specific times during the same flow cycle it is easy to visualize the pulse of 'corkscrew' type flow (Frydrychowicz, Harloff, Jung, Zaitsev, & Eigang, 2007) moving through the vessel in the spiral cases.

5 Conclusions

In this investigation a *k-ω* turbulence model has been used to model pulsatile spiral blood flow through a 75% cross sectional reduction stenosed vessel. An expected 'corkscrew' type pulse of flow has been observed downstream of the stenosis caused by the spiral components applied at the inlet boundaries. This spiral component has several observed effects on the flow properties which as mentioned in the introductory section has both beneficial and detrimental effects in the human circulator system (Stonebridge, Spiral laminar flow in arteries?, 1996) which is in agreement with the findings of this report.

The spiral component causes reduction in the turbulence intensity for both the investigated Reynolds numbers, which has a stabilising effect on the downstream region of the stenosis as suggested by previous work by Stonebridge (Stonebridge, Buckley, Thompson, Dick, Hunter, & Chudek, 2004) and Paul and Larman (Paul & Larman, 2009). This is of great pathological interest as the rise of turbulence intensity in the post stenosis region is responsible of causing damage to the blood-cell materials and to activate platelets in the blood, and subsequently, they create many pathological diseases (Ku, 1997).

A second beneficial effect was observed in the *Re* = 1000 flow case where there was a reduction of post-stenosis oscillatory shear stress in the simulation with induced spiral flow. There was no

such trend observed in the lower Reynolds number flows though. Oscillatory shear stress is known to cause potential damage to the inner side of the post-stenosis blood vessel, called endothelium (Fry, 1968).

Conversely, however, with the induction of a spiral component negative effects were also observed. An increase in pressure downstream of the stenosis was observed during the deceleration phase of the velocity pulse cycle, t = 4.40s and 4.60s, where the consequences of increased blood pressure of which are well known.

In this work, flows of Re = 500 and 1000 have been used due to their physiological relevance and use in other relevant research allowing for comparison of results. A natural extension of this piece of work would be to expand the investigation for flows of a wider range of Reynolds number. Further the model in this investigation was simplified by being considered rigid. Considering the importance of the interaction of the flow with the vessel boundaries it would be of interest to develop models of non-rigid vessels and investigate the effect of vessel surface on the induced spiral flow, as it is done by Cho et al (Cho, Kim, Sung, Ro, & Ryou, 2011) for the laminar non-spiral flow in stenosed arteries.

Acknowledgement

The authors thank the anonymous reviewers for their constructive suggestions which helped to improve the paper.

6 References

Ahmed, S. A., & Giddens, D. P. (1983). Velocity measurements in steady flow through axisymmetric stenoses at moderate Reynolds numbers. *Journal of Biomechanics, Volume 16(7)* , 505-516.

Cho, S. W., Kim, S. W., Sung, M. H., Ro, K. C., & Ryou, H. S. (2011). Fluid-structure interaction analysis on the effects of vessel material properties on blood flow characteristics in stenosed arteries under axial rotation. *Korea-Australia Rheology Journal* , 7-16.

Fluent, 6. (2007). Tutorial Guide. ANSYS Inc.

Fry, D. (1968). Acute vascular endothelial changes associated with increased blood velocity gradients. *Circ Res* (22), 65-197.

Frydrychowicz, A., Harloff, A., Jung, B., Zaitsev, M., & Eigang, E. (2007). Time-resolved,3-dimensional magnetic resonance flow analysis at 3T: visulization of narmal and pathological aortic vascular hemodynamics. *J Comput Assist Tomogr.* (22), 9-15.

Ghalici, F., Deng, X., De Chamlain, A., Douvill, Y., King, M., & Guidoin, R. (1998). Low Reynolds Number Turbulence Modeling of Blood Flow in Arterial Stenosis. *Biorheology* , 281-294.

Ku, D. (1997). Blood flows in arteries. *Annual Review of Fluid Mechanics* , 399-434.

Lam, S., Fung, G. S., Cheng, S. W., & Chow, K. (2008). A computational study on the biomechanical factors related to stent-graft models in the thoracic aorta. *Medical & Biological Engineering & Computing* , 1129-1138.

Lee, T., Liao, W., & Low, H. (2003). Numerical simulation of turbulent flow through series stenosis. *Internatial Journal for Numerical Methods in Fluids* , 717-740.

Leys, D. (2001). Atherothrombosis: a Major Health Burden. *Cerborovascular Diseases, Voll.11* , 1-4.

Patankar, S. V., & Spalding, D. B. (1972). A calculation procedure for heat, mass and momentum transfer in three-dimensional parabolic flows. *Int J Heat Mass Transfer* , 1787-1806.

Paul, M. C., & Larman, A. (2009). Investigation of spiral blood flow in a model of arterial stenosis. *Medical Engineering & Physics , 31*, 1195-1203.

Paul, M., Molla, M., & Roditi, G. (2009). Large-Eddy simulation of pulsatile blood flow. *Medical Engineering and Physics* (39), 425-36.

Ryval, J., Straatman, A. G., & Steinman, D. A. (2004). Two-equation Turbulence Modeling of Pulsatile Flow in a Stenosed Tube. *Journal of Biomechanical Engineering* , 625-635.

Sarifuddin, Chakravarty, S., Mandal, P., & Layek, G. (2008). Numerical Simulation of unsteady generalised Newtonian blood flow through differently shaped distensible arterial stenosis. *J Med Eng Technol* (32), 385-99.

Stonebridge, P. (1996). Spiral laminar flow in arteries? *Clinical Science* , 17-21.

Stonebridge, P., Buckley, C., Thompson, A., Dick, J., Hunter, G., & Chudek, J. (2004). Non spiral and spiral (helical) flow patterns in stenosis-in vitro observations using spin and gradient echo magnetic resonance imaging(MRI) and computational fluid dynamics modeling. *International Angiology; a journal of the union of international angiology , 22* (3), 276-83.

Tan, F. P., Soloperto, G., Bashford, S., Wood, N. B., Thom, S., Hughes, A., et al. (2008). Analysis of Flow Disturbances in a stenosed Carotid Artery Bifurcation Using Two-Equation Transitional And Turbulence Models. *ASME J. Biomech. Eng.* , 061008.

Wilcox, D. (1993). *Turbulence modelling for CFD.* La Canada California: DWC Industries.

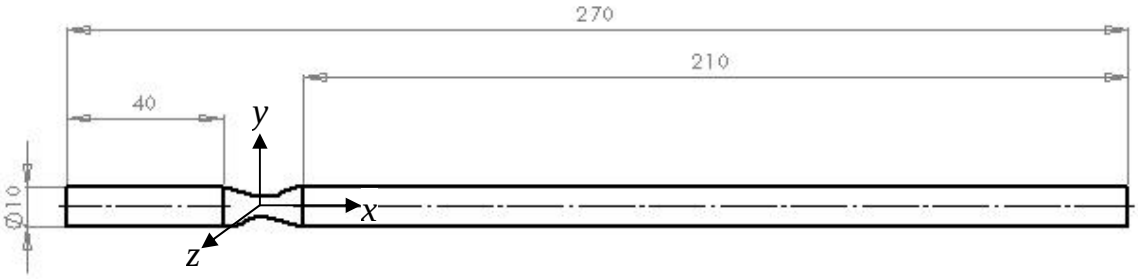

Figure 1: Diagram of stenosed vessel geometry

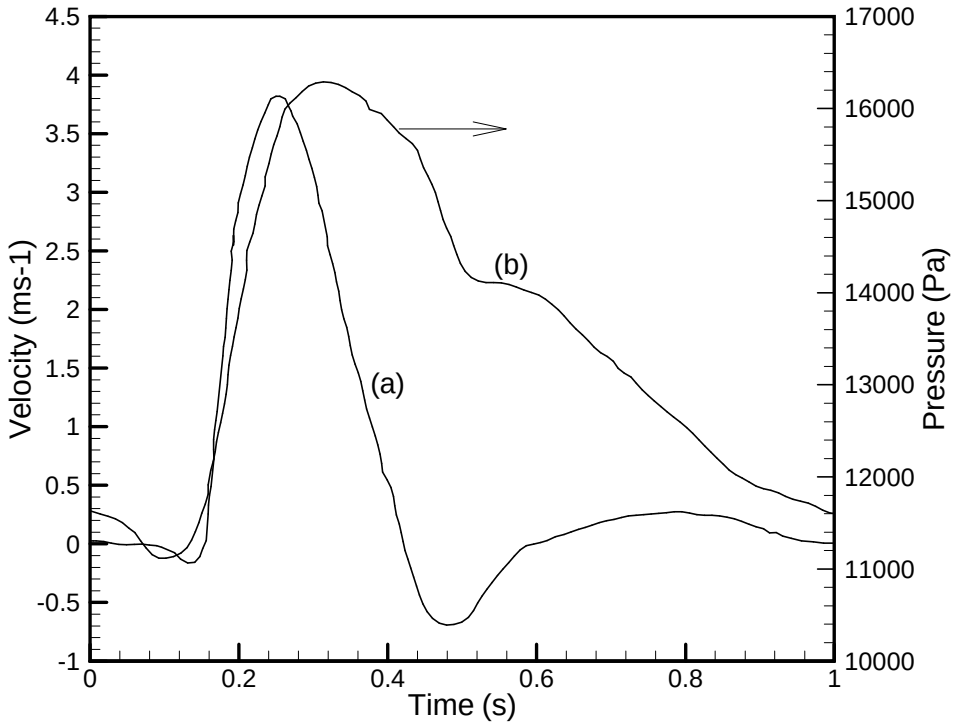

Figure 2: Blood (a) inlet velocity waveform and (b) outlet pressure waveform, Lam et al. **(Lam, Fung, Cheng, & Chow, 2008)**.

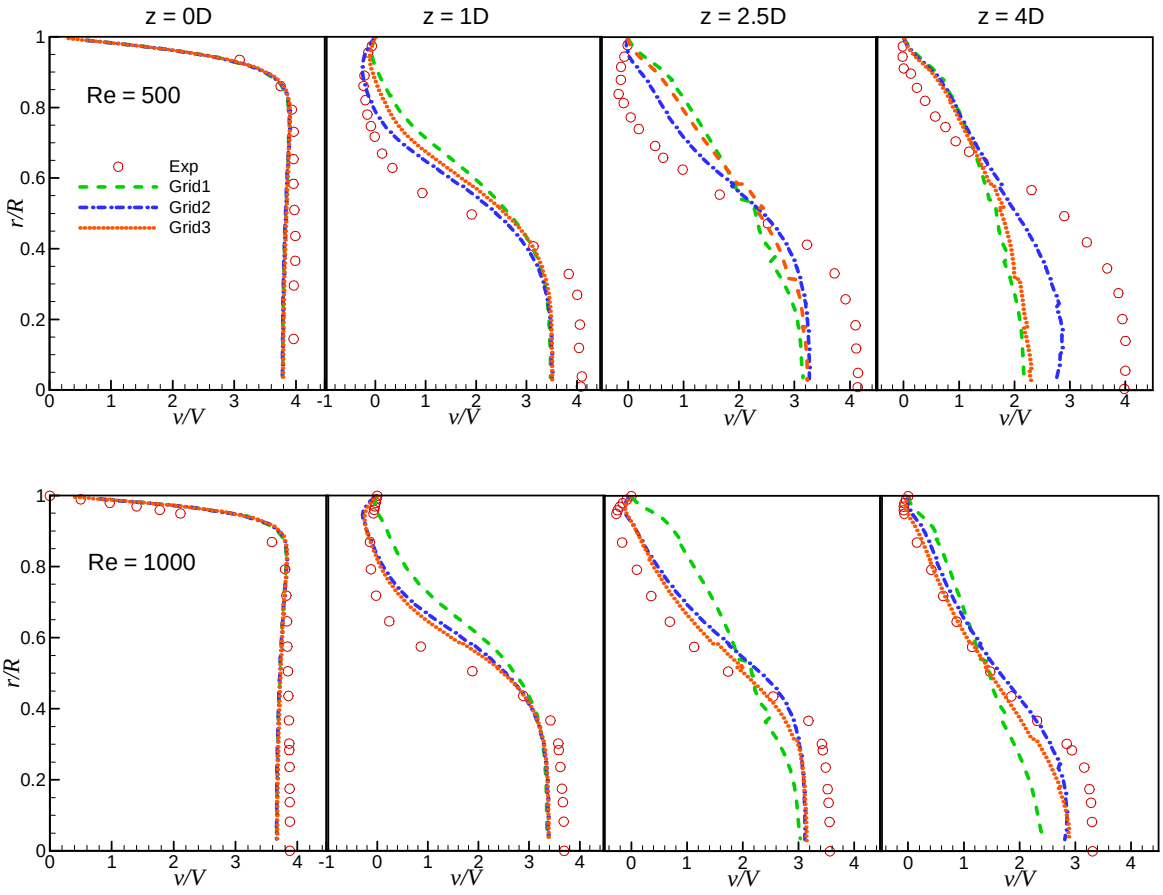

Figure 3: Mesh Independence test showing the results and experimental data of the axial velocity for *Re* = 500 and 1000 at different axial locations.

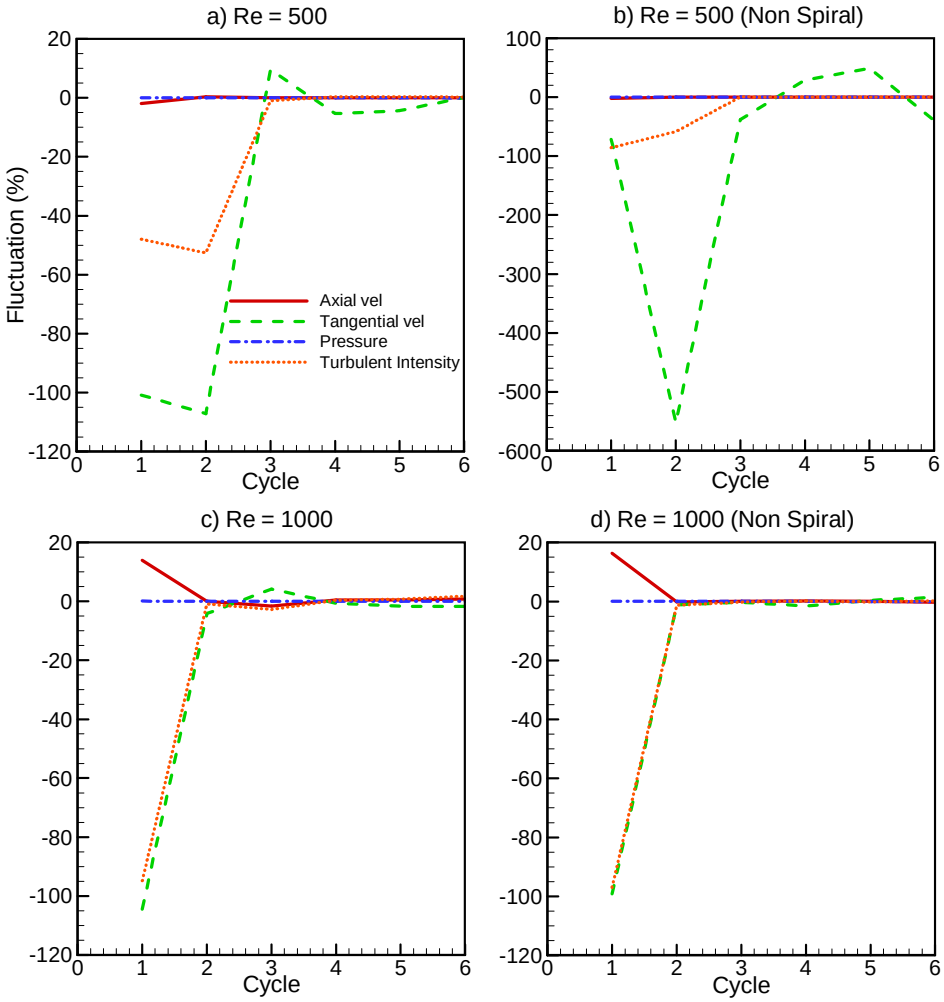

Figure 4: Fluctuation convergence of key parameters at a point z = 4D for flow conditions: (a) *Re* = 500, (b) *Re* = 500 Non-Spiral, (c) *Re* = 1000, and (d) *Re* = 1000 Non-Spiral

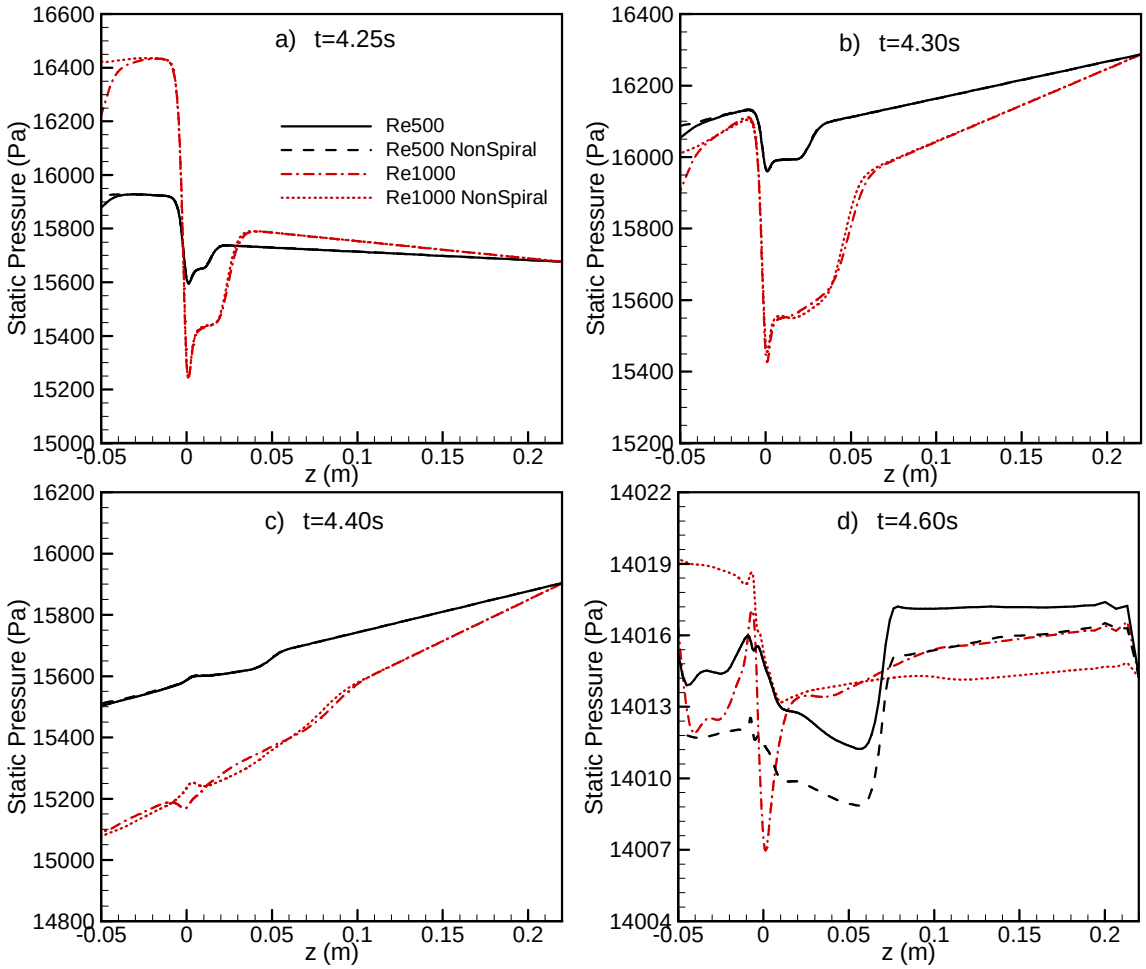

Figure 5: Variation in static pressure along the centerline for various flow conditions at times: (a) t = 4.25s, (b) t = 4.30s, (c) t = 4.40s and (d) t = 4.60s

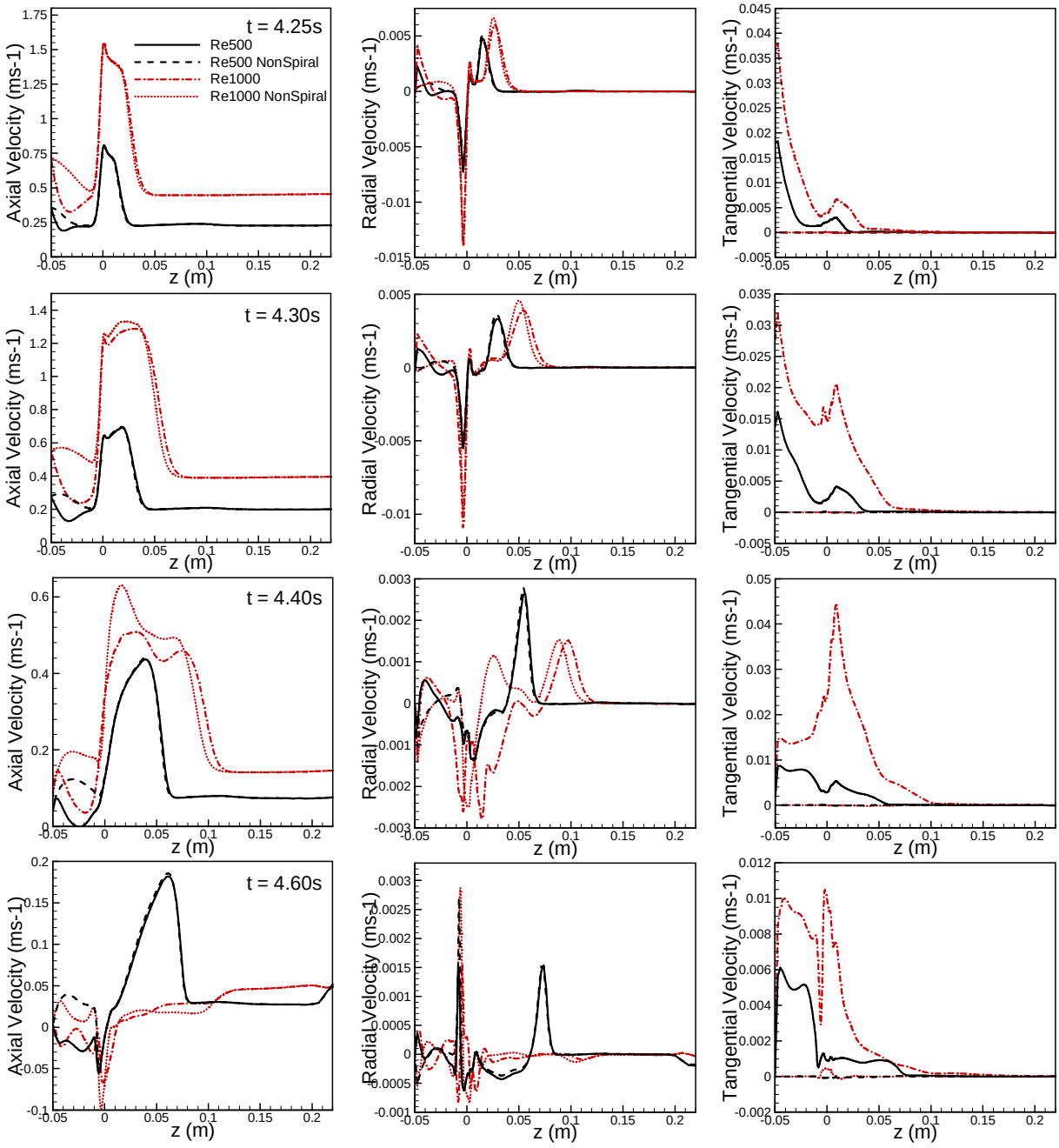

Figure 6: Variation in the axial, radial and tangential velocity along the centerline for various flow conditions at times: *t* = 4.25s, 4.30s, 4.40s and 4.60s

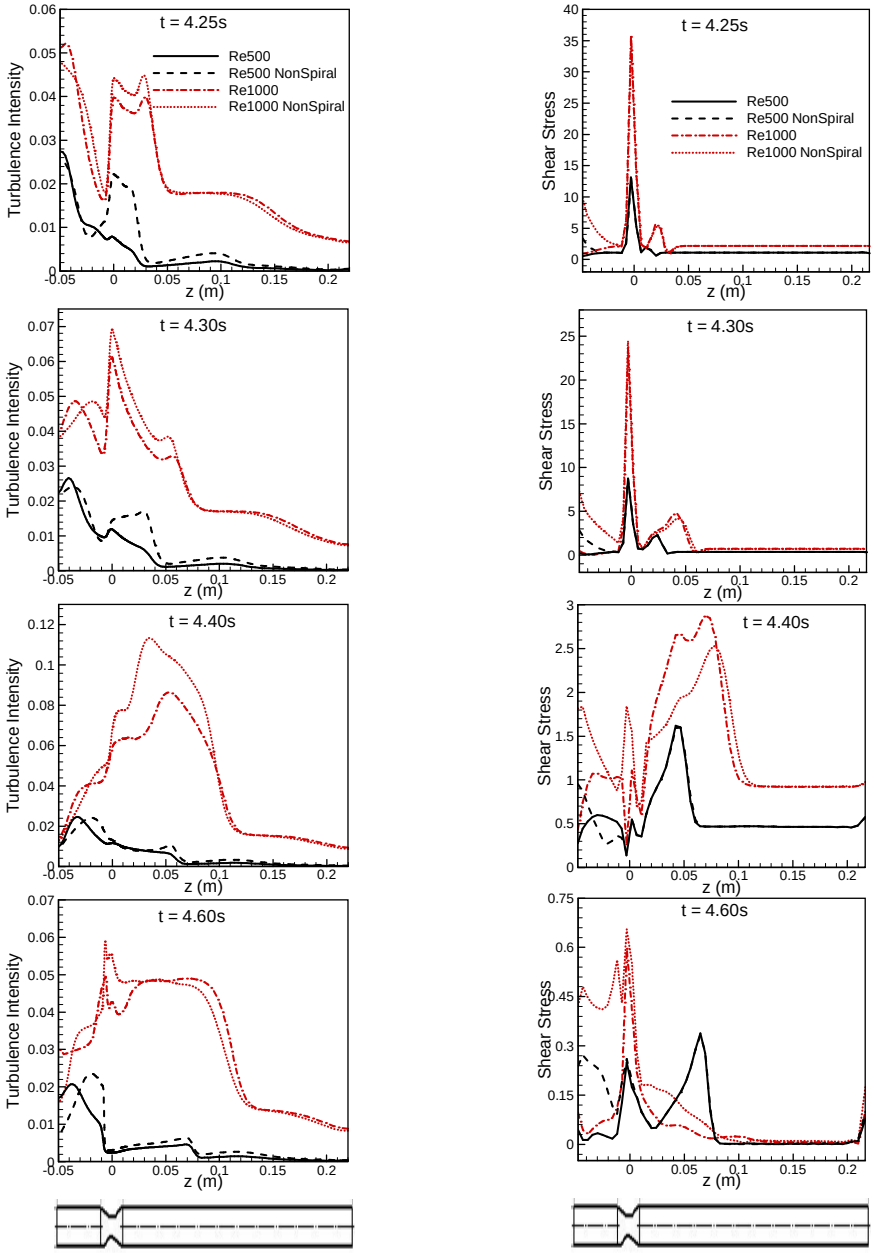

Figure 7: Variation in turbulence intensity along the centerline (left) and circumferential-average wall-shear stress (Pa) along the axial direction for various flow conditions at times t = 4.25s, 4.30s, 4.40s and 4.60s

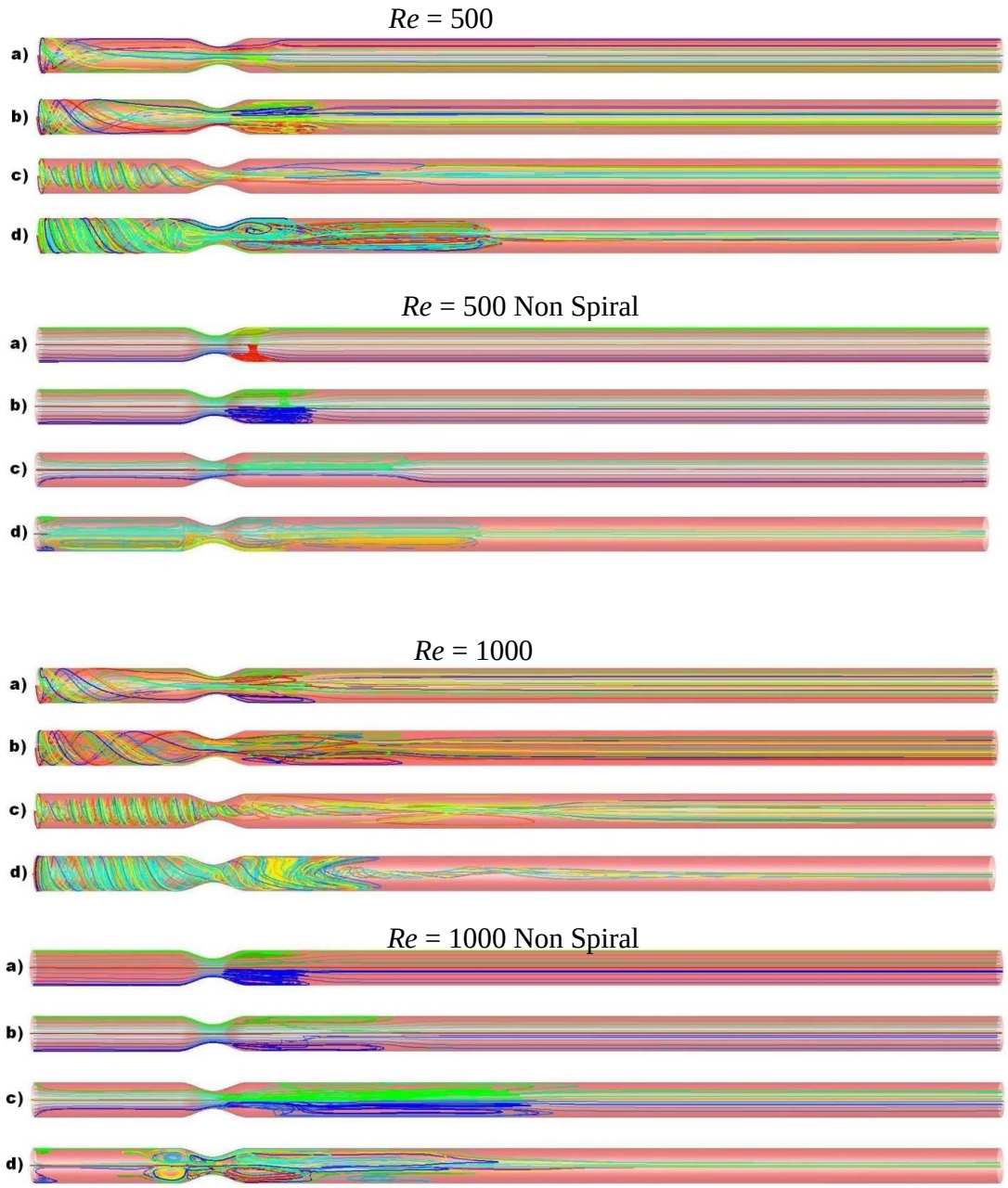

Figure 8: Pathlines coloured by particle Id during flow pulse for *Re* = 500 and 1000 at times: (a) *t* = 4.25s, (b) *t* = 4.30s, (c) *t* = 4.40s and (d) *t* = 4.60s